ACS APPLIED MATERIALS & INTERFACES

www.acsami.org

Research Article

Observation of Anisotropic Magnetoresistance in Layered Nonmagnetic Semiconducting $PdSe_2$

Rui Zhu, Zhibin Gao, Qijie Liang,* Junxiong Hu, Jian-Sheng Wang, Cheng-Wei Qiu, and Andrew Thye Shen Wee*

Cite This: *ACS Appl. Mater. Interfaces* 2021, 13, 37527−37534

Read Online

ACCESS | Metrics & More | Article Recommendations | Supporting Information

ABSTRACT: Anisotropy in crystals usually has remarkable consequences in two-dimensional (2D) materials, for example, black phosphorus, $PdSe_2$, and SnS, arising from different lattice periodicities along different crystallographic directions. Electrical anisotropy has been successfully demonstrated in 2D materials, but anisotropic magnetoresistance in 2D materials is rarely studied. Herein, we report anisotropic magnetoresistance in layered nonmagnetic semiconducting $PdSe_2$ flakes. Anisotropic magnetoresistance along the two crystalline axes under a perpendicular magnetic field is demonstrated, and the magnetoresistance along the *a*-axis is apparently different from the magnetoresistance along the *b*-axis. The magnetoresistance can also be flexibly tuned by applying a gate voltage, leveraging the semiconductor properties of $PdSe_2$. The computed anisotropic electronic density of states and electronic mobility with ab initio density functional calculations support the anisotropic and measured magnetoresistance. Our findings advance the understanding of magnetoresistance in anisotropic transition-metal dichalcogenides and pave the way for potential applications in anisotropic spintronic devices.

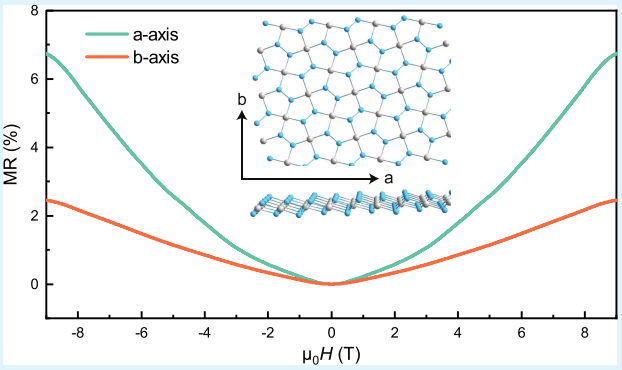

KEYWORDS: *$PdSe_2$, anisotropic magnetoresistance, anisotropic 2D materials, ab initio calculations, electronic structure, electronic mobility*

INTRODUCTION

Magnetoresistance (MR), manifesting as a change of electrical resistance induced by an external magnetic field, is used to probe the fundamental electronic properties of materials and has advanced spintronic applications.[1] Anisotropic MR (AMR) measures the dependence of resistance on the angle between the direction of electric current and magnetization or the angle between the crystal axis and magnetization. AMR is mainly observed in two kinds of materials. The first kind is ferromagnets and antiferromagnets[2−4] in which AMR arises from their magneto-crystalline anisotropy energy. The second kind is some topological semimetals and materials[5−7] in which AMR arises from the field-dependent current induced by the chiral anomaly of Dirac and Weyl fermions or the Berry curvature in topological metals. Under these conditions, the AMR ratio is mainly dependent on the applied magnetic field and the application of such a phenomenon is based on the rotation of the magnetic field. Until now, the AMR phenomenon has been successfully applied in magnetic sensors.[8] Exploring intrinsic AMR independent of the rotation of magnetization could have important device applications.

Two-dimensional (2D) materials have been extensively investigated due to their potential applications in next-generation electronic and spintronic devices.[9−12] The study of in-plane anisotropic 2D materials began with black phosphorous in 2014 followed by other anisotropic 2D materials, which can be classified into semimetals (e.g., Td-WTe_2[13] and $ZrTe_5$[14]) and semiconductors (e.g., SnS,[15] GaTe,[16] and $PdSe_2$[17]). Arising from their anisotropic atomic structure, unique physical properties have been demonstrated, including anisotropic optical absorption, anisotropic electrical conductance, anisotropic thermal transport, and anisotropic mechanical properties. MR investigations of 2D materials have been only limited to a few 2D materials, including semimetals such as graphene,[18,19] Td-WTe_2,[20,21] and $PtSe_2$[22] or semiconductors such as 2H-WS_2[23] and 2H-$MoSe_2$.[24] However, there has been few reports of the MR phenomenon in anisotropic semiconductors, such as black phosphorous.[25,26]

Received: June 6, 2021
Accepted: July 26, 2021
Published: August 1, 2021

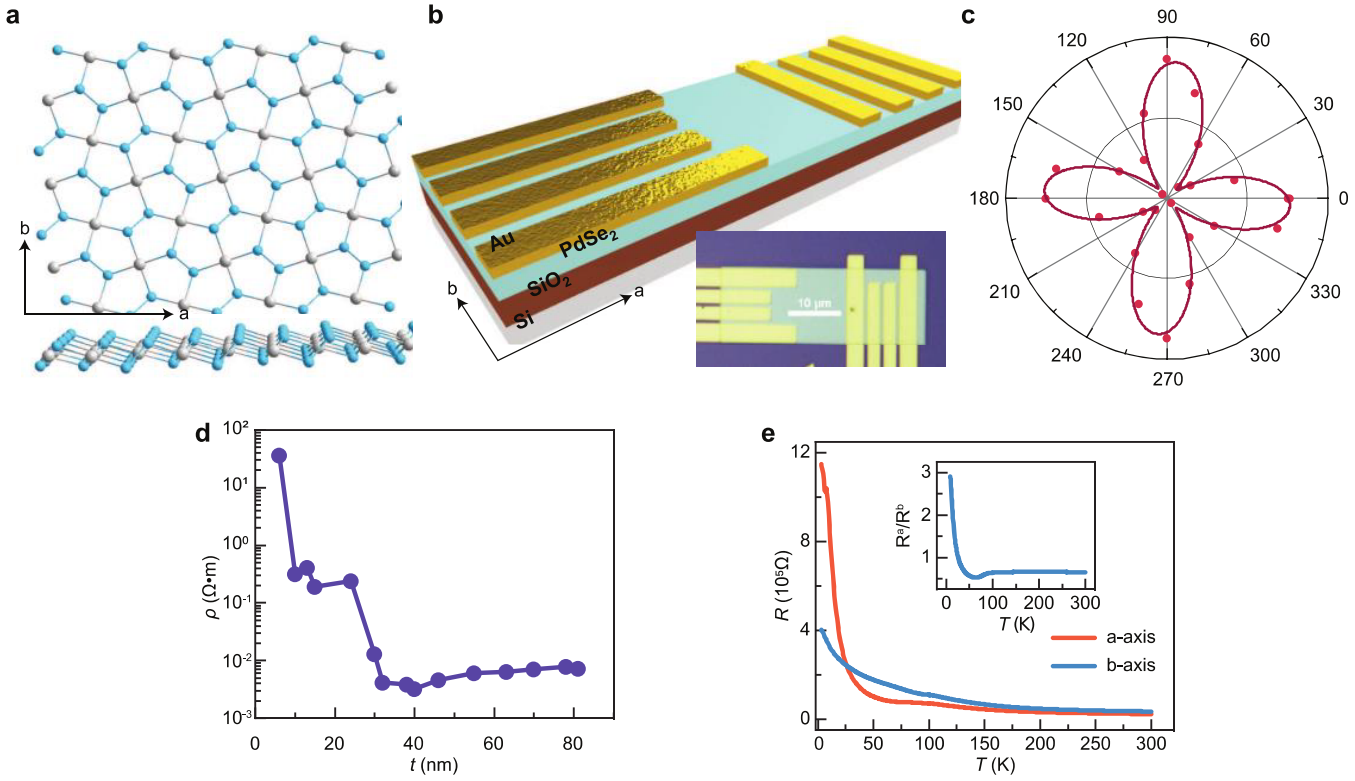

Figure 1. Characterization of trivial bulk $PdSe_2$. (a) Atomic crystal structure of $PdSe_2$. (b) Schematics of an exfoliated $PdSe_2$ device on a SiO_2/Si substrate with parallel electrodes along the *a*-axis and *b*-axis and the corresponding optical microscope image (the long edge corresponds to the *a*-axis while the short edge corresponds to the *b*-axis). (c) Polar plots of peak intensities of the A_g mode as a function of polarization angle under the parallel configuration. (d) Resistivity of the exfoliated $PdSe_2$ flakes versus their thickness determined using an AFM at 300 K. (e) Temperature dependence of the resistance along the *a*-axis and *b*-axis under zero magnetic field. The inset shows the extracted ratio of resistance along *a*-axis to *b*-axis as a function of temperature from 3 to 300 K.

Pentagonal $PdSe_2$, a noble transition-metal dichalcogenide (TMD), has been attracting increasing attention in the recent 5 years.[27] The structure of $PdSe_2$ features pentagonal bonding, resulting in a lack of rotational symmetry.[28,29] $PdSe_2$ presents in-plane anisotropic properties similar to black phosphorous, thus having direction-dependent physical properties such as mechanical flexibility, carrier mobility, thermal conductivity, and optical responsivity. These unique physical properties and applications based on $PdSe_2$ have been reported by several groups. The atomic structure and defects of pristine $PdSe_2$ were studied by scanning tunneling microscopy.[30] A high-performance broadband photodetector based on $PdSe_2$ has been realized,[31] demonstrating high responsivity (up to 708 AW^{-1}) and photogain (G) (up to 82,700%) in the visible, near-infrared, and mid-infrared range. A large tunable band gap was achieved by varying the thickness of $PdSe_2$, and the band gap was reported to change from 1.15 to 0.55 eV as the thickness was varied from 2 layers to 26 layers.[30] Anisotropic phonon responses of $PdSe_2$ under different strains,[32] oxygen substitution of Pd atoms,[33] and linear dichroism transition[34] have also been investigated. Nevertheless, there have been few reports on the MR of $PdSe_2$ so far. Investigating the MR in $PdSe_2$ is important for understanding its physical properties as well as for applications in memory and spintronic devices.

Herein, we successfully demonstrated a robust MR phenomenon in exfoliated $PdSe_2$ flakes. When we aligned the magnetic field out of the sample plane, abnormal AMR was observed along the two crystalline axes, *a*-axis and *b*-axis, attributed to the anisotropic atomic structure of $PdSe_2$. In addition, a crossover from positive MR to negative MR was observed with the increasing temperature. Moreover, benefiting from the semiconducting properties, gate controllability of the magnitude of MR is demonstrated. Finally, we performed density functional theory (DFT) calculations to explore the microscopic origin of this observed abnormal AMR.

RESULTS AND DISCUSSION

Selection and Fabrication of $PdSe_2$ Devices. Pentagonal $PdSe_2$, a noble TMD, presents in-plane anisotropic properties as black phosphorus. The crystal structure of $PdSe_2$ features unique pentagonal bonding as shown in Figure1a and possesses two inequivalent major crystal axes ([100] and [010]) along the *a* and *b* directions in the 2D plane, respectively. Micromechanical exfoliation was used to prepare $PdSe_2$ flakes on SiO_2/Si substrates with different thicknesses from single-crystalline bulk $PdSe_2$. One piece of exfoliated $PdSe_2$ flake is shown in Figure 1b, from which we can see it features a distinct long strip shape, indicating the preferred cleaving direction of bulk $PdSe_2$. This flake is 38 nm as measured using an atomic force microscope (Figure S1). According to a previous study,[35] the long edge corresponds to the *a*-axis ([100] direction) whereas the short edge aligns with the *b*-axis ([010] direction). Figure1b shows the schematic of the $PdSe_2$ devices, where two groups of parallel electrodes are fabricated to obtain longitudinal resistance along the *a*-axis and *b*-axis, respectively. Polarized Raman spectroscopy was used to identify the in-plane anisotropy of $PdSe_2$. As for the Raman spectra of this $PdSe_2$ flake shown in Figure S2, the vibrational

https://doi.org/10.1021/acsami.1c10500
ACS Appl. Mater. Interfaces 2021, 13, 37527−37534

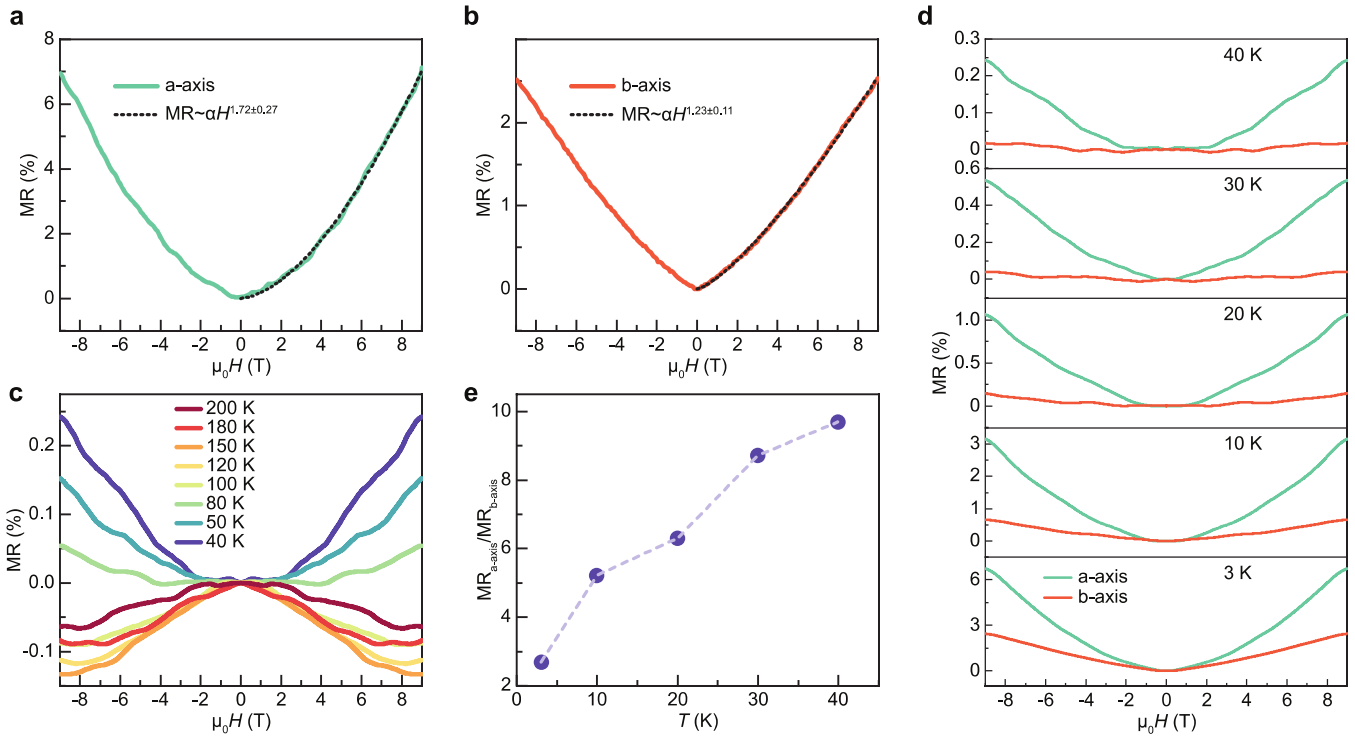

Figure 2. AMR along two axes for trivial bulk $PdSe_2$. (a) Solid line showing MR along the *a*-axis as a function of the magnetic field while the dashed line is the fitting curve. (b) Solid line representing MR along the *b*-axis, which is fitted by a nearly linear curve shown by the dashed line. (c) MR along the *a*-axis from 40 to 200 K. (d) Comparison of MR along the *a*-axis and *b*-axis at various temperatures from 3 to 40 K. (e) Ratio of MR along *a*-axis to *b*-axis at 9 T under different temperatures extracted from panel (d).

modes at 151, 213, and 264 cm^{-1} correspond to the A_g peaks and that at 229 cm^{-1} can be assigned to the contribution of the B_{1g} mode, consistent with the previous study.[32] The angle-dependent Raman peak intensity of the A_g mode at 151 cm^{-1} is plotted in Figure 1c. The dominant orientations of the maxima differ by 90°, corresponding to the *a*-axis and *b*-axis, respectively, verifying the inherent in-plane anisotropy of $PdSe_2$. The resistance of $PdSe_2$ is highly dependent on thickness since it shows an apparent layer-dependent band gap.[30] The resistivity of exfoliated $PdSe_2$ flakes with different thicknesses was measured at 300 K as shown in Figure 1d, and it drops sharply at first and then becomes stable, parallel with the thickness-dependent band gap.[36] After carefully checking the resistivity of ultrathin $PdSe_2$ flakes under a different magnetic field, no remarkable MR was found due to the giant resistivity and low electron mobility in these flakes. Although bulk $PdSe_2$ exhibited a zero band gap as shown in Figure S3 based on the ab initio density functional electronic structure calculations that agree with the previous study,[17] trivial bulk $PdSe_2$ still exhibited a narrow band gap where the trivial bulk has a thickness between atomically thin and bulk. Thus, we selected trivial bulk $PdSe_2$ flakes with thicknesses of 35−50 nm in this study, corresponding to a 0.5 eV band gap of $PdSe_2$.[36] Figure 1e shows the resistance along the *a*-axis and *b*-axis as a function of temperature for this 38 nm $PdSe_2$. The resistance for both the *a*-axis and *b*-axis increased as the temperature decreased, suggesting the semiconductor behavior of this $PdSe_2$ flake, in accordance with other semiconducting 2D materials. The overall measured resistance was within a relatively small value range from 300 to 3 K, facilitating the investigation of the MR behavior. Similar to the conventional in-plane anisotropic materials such as GaTe,[16] the electronic transport properties of trivial bulk $PdSe_2$ were anisotropic along different crystal axes. To observe this anisotropy intuitively, the resistance ratio along the two axes (R_a/R_b) is shown in the inset of Figure 1e. The resistance ratio is about 0.5 at 300 K and reaches 3 at 3 K. This value is comparable with other reported anisotropic conductance ratios, for example, SnS.[15] However, to our knowledge, there have been no MR investigations on these in-plane anisotropic TMDs taking their large resistances and overall thicknesses into consideration. Moreover, we extracted a lower bound of the band gap of $PdSe_2$ from the Arrhenius plot using $\frac{1}{R} \propto \exp\left(-\frac{E_g}{2kT}\right)$, where E_g is the transport band gap and k is the Boltzmann constant. After fitting the curve of $\ln \frac{1}{R}$ versus $\frac{1000}{T}$ as shown in Figure S4, we extracted a band gap of 0.345 ± 0.027 eV, which is lower than the reported value of 0.5 eV since this method omits the contribution from trap states. DFT was used to determine the band gap of trivial bulk $PdSe_2$. Our calculated band gap of trivial bulk $PdSe_2$ is in accordance with the experimental band gap obtained from reflectance spectra, which will be discussed later. The phonon dispersion without a negative frequency is shown in Figure S5, indicating the dynamical stability of our bulk $PdSe_2$ structures and samples.

Experimental Observation of AMR in Semiconducting $PdSe_2$. To gain insights into the MR of $PdSe_2$, we examined the transverse MR along the *a*-axis and *b*-axis at 3 K as shown in Figure 2a,b, respectively, where the magnetic field was applied perpendicular to the sample plane, and MR as a function of the magnetic field is described by the field-dependent resistance $\mathrm{MR} = \frac{R_H - R_{H=0}}{R_{H=0}} \times 100\%$. The MR curves

https://doi.org/10.1021/acsami.1c10500
ACS Appl. Mater. Interfaces 2021, 13, 37527−37534

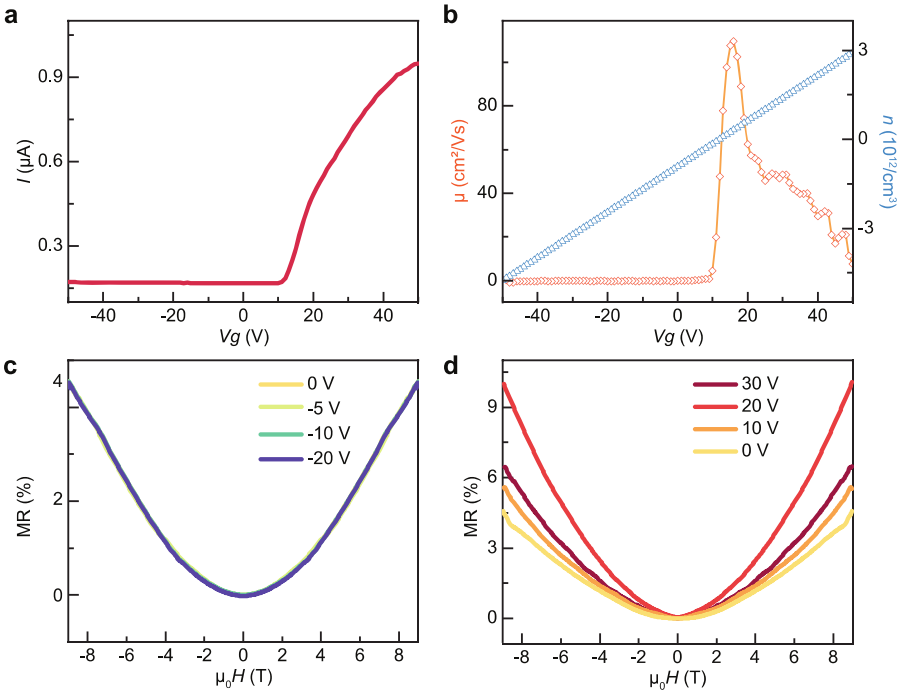

Figure 3. Gate-tunable MR along the *a*-axis. (a) Drain current as a function of back gate voltage for a trivial bulk $PdSe_2$ device with a 0.1 V drain bias at 3 K. (b) Electron mobility and concentration versus back gate voltage. (c) MR as a function of magnetic field under gate voltages corresponding to the "off-state" at 3 K. (d) MR versus magnetic field under different gate voltages from 0 to 30 V.

can be fitted using the Kohler scaling law $\mathrm{MR} = \alpha\left[\frac{\mu_0 H}{R_{H=0}}\right]^m$. As shown by the dashed line in Figure 2a, the MR data at 3 K fit the $\mathrm{MR}\sim\alpha H^m$ curve very well, with $m = 1.72 \pm 0.27$ obtained by the fitting. The MR can reach 7×100% at 3 K and 9 T and does not show any sign of saturation up to the highest field 9 T in the physical property measurement system (PPMS). While for the *b*-axis, a nonsaturating linear field dependence of MR occurs. Referring to the dashed line shown in Figure 2b, the MR data at 3 K coincide with the $\mathrm{MR}\sim\alpha H^{1.23 \pm 0.12}$ curve, confirming that MR has a nearly linear field dependence. The observation of nonsaturating MR in this nonmagnetic trivial bulk $PdSe_2$ can be explained by the Parish−Littlewood (PL) model,[37] which attributes the appearance of MR to the spatial fluctuation of carrier mobility in a disordered crystal. Furthermore, the relationship between the MR and magnetic field is maintained with increasing temperature. Figure 2c shows the transverse MR along the *a*-axis from 3 to 200 K. The MR maintains a near quadratic field dependence in this temperature range. What is surprising is that there exists a positive MR to negative MR crossover. When the temperature is below 80 K, the transverse MR is positive, with the magnitude decreasing with an increase in temperature. When it is further increased beyond 100 K, the MR becomes negative. This crossover is ascribed to the suppression of thermal spin fluctuations under the magnetic field in ferromagnets.[38] However, trivial bulk $PdSe_2$ is a nonmagnetic semiconductor. This kind of crossover is also observed in WS_2,[23] and the appearance of the crossover from positive to negative MR in $PdSe_2$ is attributed to scattering in the highly disordered crystal, in agreement with the PL model.[37] A similar behavior is observed for the *b*-axis as shown in Figure S6. Although the angle between the *a*-axis and the magnetic field is the same as the angle between the *b*-axis and the magnetization direction, abnormal AMR along the *a*-axis and *b*-axis can still be observed. To see the difference between MR along the two axes more intuitively, we merged the MR curves along the two axes in one figure as shown in Figure 2d (bottom panel). An obviously different MR behavior was observed in the magnetic field. In addition, MR curves along the two axes at other temperatures are shown in Figure 2d, from which abnormal AMR along the two axes can be observed from 3 to 40 K. We extracted the ratio of MR along *a*-axis to b-axis ($\mathrm{MR}_{a\text{-axis}}/\mathrm{MR}_{b\text{-axis}}$) at 9 T from Figure 2d and plotted it as shown in Figure 2e. It can be clearly seen that the difference is sustained and even becomes larger with increasing temperature as the ratio varies from 2 to 10. The intrinsic mechanism of the observed anomalous AMR in $PdSe_2$ is attributed to the anisotropic atomic structure, inducing anisotropic carrier mobility along the two axes, which we will discuss in detail later.

Gate Voltage Dependence of the MR Signals. Gate doping is an efficient method to tune the electronic properties of 2D materials.[39] Due to the semiconductor properties of trivial bulk $PdSe_2$, we can continuously tune the carrier concentration in $PdSe_2$ by applying a gate voltage, which is a direct method for tuning the MR magnitude. To elucidate the relationship between gate voltage and MR, we measure another Hall bar device based on about 40 nm $PdSe_2$. The four-terminal resistance along the *a*-axis versus the back gate voltage measured at different temperatures for this device under a zero magnetic field is plotted in Figure S7. The transfer curve shows a bipolar behavior at high temperatures and an n-type semiconductor behavior with decreasing temperature. At 300 K, the maximum resistance is observed at 0 V. Owing to its high conductivity at 300 K, the electronic tuning of the Fermi level is challenging, leading to an ultrasmall on-off ratio. With the decrease of temperature, the on-off ratio increases, making it feasible to tune the electronic properties using a gate voltage. Here, we focus on the MR along the *a*-axis at 3 K due to the

https://doi.org/10.1021/acsami.1c10500
ACS Appl. Mater. Interfaces 2021, 13, 37527−37534

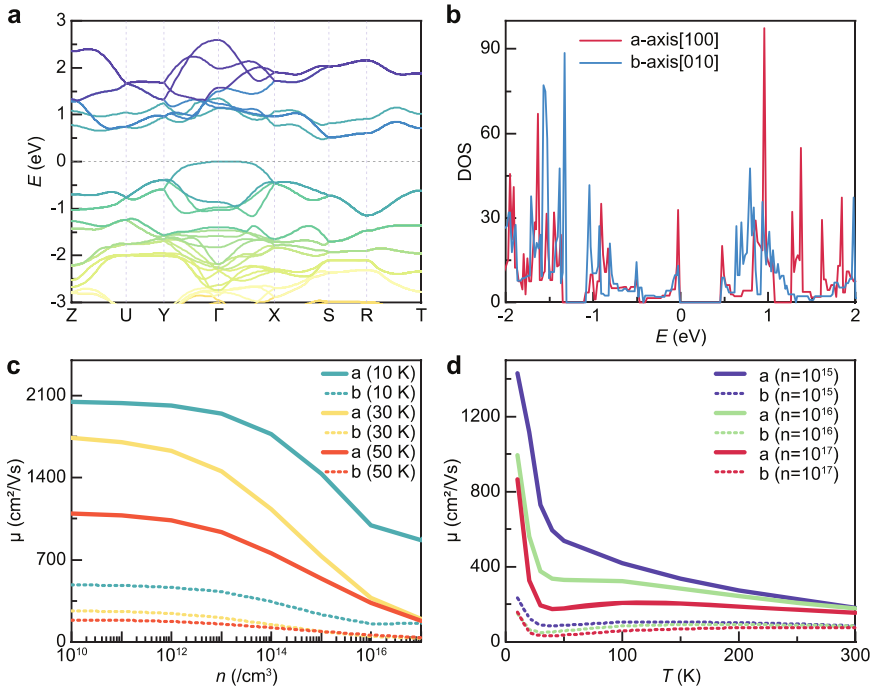

Figure 4. DFT calculations of $PdSe_2$. (a) Calculated electronic band structure of trivial bulk $PdSe_2$ with a 0.5 eV band gap at the DFT-PBE level. The Fermi level is set at the maximum of the valence band. (b) In-plane DOS along the *a*-axis and *b*-axis. (c) Calculated electron mobility as a function of electron concentration with the boundary effect. (d) Temperature-dependent electron mobility with various electron concentrations for the *a*-axis and *b*-axis with the boundary effect, which means that we consider the scattering from the acoustic deformation potential phonons, polar optical phonons, and boundary scattering.

relatively larger magnitude compared with that along the *b*-axis. To investigate the transport properties of this trivial bulk $PdSe_2$, field-effect transistor devices were measured. Figure 3a shows the plot of the drain current as a function of back gate voltage for the trivial bulk $PdSe_2$ device with a 0.1 V drain bias at 3 K. The device exhibits a typical n-type semiconductor behavior. The apparent field-effect mobility can be extracted from this transfer curve using the equation $\mu = \left(\frac{L}{WC_{ox}V_{sd}}\right)\left(\frac{dI}{dV_g}\right)$, where L and W are the channel length and width, respectively. C_{ox} is the capacitance per unit area between the channel and the back gate voltage given by $C_{ox} = \frac{\varepsilon_0\varepsilon_r}{d}$, where $\varepsilon_0 = 8.85 \times 10^{-12}$ Fm^{-1}, $\varepsilon_r = 3.9$, and $d = 280$ nm. The gate-tuned carrier concentration can be obtained from the equation $n = \frac{C_{ox}(V_g - V_{th})}{q}$, where V_{th} represents the threshold voltage. The extracted electron mobility and concentration are plotted in Figure 3b. The maximum electron mobility can reach 108 cm^2/Vs at 17 V for the *a*-axis at 3 K. The same method is used to measure the electron mobility from 3 to 300 K as shown in Figure S8a in which the electron mobility decreases with the temperature increase, in agreement with the calculated mobility shown in Figure 4d. To examine the influence of the gate voltage on the magnitude of MR, we measured MR along the *a*-axis under various gate voltages. Figure 3c shows the MR curve under gate voltages corresponding to the "off-state" in the transfer curve. All the lines coincide in this case. When we further increased the gate voltages, an enhanced MR was observed as shown in Figure 3d. The maximum MR reaches 10% under a 20 V gate voltage at 9 T. The MR magnitude shows a positive correlation with electron mobility, consistent with the PL model.[37]

DFT Considerations and Microscopic Calculations. Figure 4a shows the plot of the calculated electronic band structures, from which we can find that trivial bulk $PdSe_2$ exhibits a 0.48 eV band gap, in accordance with the experimental band gap obtained from the reflectance spectra.[36] Before discussing the microscopic physics of the AMR observed in trivial bulk $PdSe_2$, we first recall the fundamentals of the conventional AMR in semiconducting ferromagnets and antiferromagnets. For a noncrystalline AMR component, the AMR depends only on the angle between magnetization and current. As for the pure crystalline AMR, it is determined by the varying angle between magnetization and crystal axes. However, the observed AMR in trivial bulk $PdSe_2$ is solely dependent on which crystal axes the current is applied, while independent of the angle between magnetization and current or crystal axes. We will explain this abnormal AMR from the aspects of the anisotropic density of states (DOS) and anisotropic electronic mobility.

The anisotropy of the electronic structure with respect to the anisotropy of the DOS gives a quantitative description of the measured transport behavior. To analyze the electronic structure anisotropy phenomena, we performed DFT aligned along the *a*-axis and *b*-axis crystal axes. Figure 4b shows the plot of the calculated in-plane DOS along the two axes, $DOS_{a\text{-axis}}$ and $DOS_{b\text{-axis}}$. Large overall DOS anisotropies, a remarkable anisotropy in the band gap, and strong energy dependence of the DOS anisotropy can be found. Since the $PdSe_2$ crystal property is very sensitive to the thickness and the number of layers, we systematically optimized the bulk $PdSe_2$ with the accessible different functionals, as shown in Table S1. The optimized lattice using the PBE-SCAN+rVV10 method[40] (a = 5.7419 Å, b = 5.8667 Å, and c = 7.7307 Å) is almost

https://doi.org/10.1021/acsami.1c10500
ACS Appl. Mater. Interfaces 2021, 13, 37527−37534

identical compared to the experimental data with a = 5.7457 Å, b = 5.8679 Å, and c = 7.6946 Å.[41]

The MR in nonmagnetic $PdSe_2$ originates from the spatial fluctuation of carrier mobility. Thus, the anisotropic electron mobility along the a-axis and b-axis is the possible origin of the abnormal AMR. Figure 4c shows electron mobility along the a-axis and b-axis as a function of electron concentration with the boundary effect, and the obviously different electron mobilities along the two axes can be seen for various electron concentrations. The dependence of electron mobility on electron concentrations also demonstrates the validity of gate controllability for the magnitude of MR. Figure 4d shows the plot of the temperature-dependent electron mobility for the a-axis and b-axis with the boundary effect in which the variation tendency is consistent with the experimental data although specific values differ from the experiments since the contribution of defects cannot be estimated at the DFT level. For comparison, electron mobility without the boundary effect is also shown in Figure S9. The value is larger than that considering the boundary effect. However, in both cases, remarkable anisotropic mobilities along the a-axis and b-axis can be found, in agreement with our experimental measurement shown in Figure S8b.

CONCLUSIONS

In summary, we present a comprehensive investigation of MR in semiconducting trivial layered $PdSe_2$ flakes. The unique pentagonal crystal structure of $PdSe_2$ leads to the anomalous anisotropic in-plane MR, where the MR along the a-axis differs notably from that along the b-axis when the magnetic field is perpendicular to the sample plane. Furthermore, the magnitude of the positive transverse MR can be modulated by applying a gate voltage due to the semiconducting nature of the exfoliated trivial bulk $PdSe_2$ flakes. Our computed anisotropic electronic DOS and electronic mobility with ab initio DFT calculations further explain the AMR in the experimental measurements. This study provides us a deeper understanding of MR in anisotropic-layered TMDs. It also helps us to understand the fundamental properties of $PdSe_2$ and paves the way for potential applications in anisotropic memory and spintronic devices.

METHODS

Device Fabrication and Characterization. The $PdSe_2$ flakes were prepared by micromechanically exfoliating $PdSe_2$ from a bulk crystal (2D semiconductor) onto a SiO_2 (280 nm)/Si substrate. The electrode contacts were patterned by electron beam lithography (FEI EBL). After this, Ti/Au (5/100 nm) was deposited by electric beam evaporation and liftoff was performed in acetone. Atomic force microscopy (AFM) measurements under the tapping mode were conducted with an AFM (Bruker) in an ambient environment to determine the thickness of the exfoliated flake. Raman spectra were collected using a commercial WITec Raman system using a 532 nm laser. A polarizer was placed between the edge filter and a detector to obtain a parallel polarization configuration.

Electrical Transport Measurements. The electrical transport measurements were carried out using a PPMS interfaced with a source meter (Model 2400, Keithley Inc.) and a multimeter (Model 2002, Keithley Inc.). A direct current of 0.5 μA was applied through the sample to measure the longitudinal resistance in the magnetic field (perpendicular to the sample plane) with the magnitude varying from −9 to 9 T.

Computational Details. The crystal structure of $PdSe_2$ was optimized using the projector augmented wave pseudopotentials, local density approximation,[42] and Perdew−Burke−Ernzerhof (PBE) functionals as implemented in the VASP code.[43] In addition, we also systematically tested other different functionals including vdW interactions as shown in Table S1. A cutoff with 550 eV energy and 15 × 15 × 15 samplings was adopted. The criterion of convergence for electronic band structures, DOS, elastic constants, dielectric constants, and phonon dispersions are 1×10^{-8} eV and 1×10^{-4} eV/Å. The phonon dispersion curve was calculated using the Phonopy.[44]

In the framework of the Boltzmann transport theory, the electronic conductivity can be calculated as[28]

$$\sigma = \frac{2e^2}{8\pi^3}\sum_i \int d^3\vec{k}\cdot\tau_i(\vec{k})\cdot\vec{v}_i(\vec{k}) \otimes \vec{v}_i(\vec{k})\cdot\left[-\frac{\partial f(\mu, T, \varepsilon_i)}{\partial \varepsilon_i}\right]$$

where 2 is the spin degeneracy and $\vec{v}_i(\vec{k})$ is the electron group velocity with a wave vector $\vec{k}$ and band index i. ε_i, μ, and $\tau_i(\vec{k})$ are electronic energy, chemical potential, and electronic relaxation time. Therefore, the only unknown parameter to obtain conductivity is the electronic relaxation time. Using Fermi's golden rule, the scattering rate (inverse of relaxation time) from state $|n\vec{k}\rangle$ to state $|m\vec{k} + \vec{q}\rangle$ can be calculated as

$$\tau^{-1}_{n\vec{k}\to m\vec{k}+\vec{q}} = \frac{2\pi}{\hbar}|g_{nm}(\vec{k}, \vec{q})|^2\,\delta(\varepsilon_{n\vec{k}} - \varepsilon_{m\vec{k}+\vec{q}})$$

in which $g_{nm}(\vec{k}, \vec{q})$ is the matrix element for scattering from the state $|n\vec{k}\rangle$ to state $|m\vec{k} + \vec{q}\rangle$. The specific formula of the scattering matrix element can be further written for each scattering mechanism. Here, we consider acoustic deformation potential scattering, polar optical phonon scattering, and boundary scattering.

The scattering rate of acoustic deformation potential scattering is defined as[45]

$$g^{acd}_{nm}(\vec{k}, \vec{q}) = \sqrt{k_B T}\sum_{\vec{G}\neq -\vec{q}}\left[\frac{D{\sim}_{n\vec{k}}\cdot\hat{S}_l}{c_l\sqrt{\rho}} + \frac{D{\sim}_{n\vec{k}}\cdot\hat{S}_{t_1}}{c_{t_1}\sqrt{\rho}} + \frac{D{\sim}_{n\vec{k}}\cdot\hat{S}_{t_2}}{c_{t_2}\sqrt{\rho}}\right]\langle m\vec{k} + \vec{q}|e^{i(\vec{q}+\vec{G})\cdot\vec{r}}|n\vec{k}\rangle$$

where $D{\sim}_{n\vec{k}} = D_{n\vec{k}} + \vec{v}_i(\vec{k}) \otimes \vec{v}_i(\vec{k})$ in which $D_{n\vec{k}}$ is the deformation potential tensor. $S = \hat{q} \otimes \hat{u}$, where $\hat{u}$ is the unit vector of phonon polarization. The subscripts l, t_1, and t_2 indicate properties related to the longitudinal and transverse modes, respectively.

The scattering rate of polar optical phonon scattering is defined as[46]

$$g^{po}_{nm}(\vec{k}, \vec{q}) = \left[\frac{\hbar\omega_{po}}{2}\right]^{1/2}\sum_{\vec{G}\neq -\vec{q}}\left[\frac{1}{\hat{n}\cdot\epsilon_\infty\cdot\hat{n}} - \frac{1}{\hat{n}\cdot\epsilon_s\cdot\hat{n}}\right]^{1/2}\frac{\langle m\vec{k} + \vec{q}|e^{i(\vec{q}+\vec{G})\cdot\vec{r}}|n\vec{k}\rangle}{|\vec{q} + \vec{G}|}$$

where ϵ_s and ϵ_∞ are the static and high-frequency dielectric tensors and ω_{po} is the polar optical phonon frequency.

The scattering rate of boundary scattering is defined as

$$g^{bo}_{nm}(\vec{k}, \vec{q}) = \sum_{\vec{G}\neq -\vec{q}}\frac{\vec{v}_{ii}(\vec{k})}{L}\langle m\vec{k} + \vec{q}|e^{i(\vec{q}+\vec{G})\cdot\vec{r}}|n\vec{k}\rangle$$

where L is the grain size of the sample. Here, we use the typical boundary size of 20 nm, which has been experimentally proved in other systems such as MoS_2 films.[47] Although we cannot accurately measure the grain size in the samples, this typical size also in layered MoS_2 can still help us to further understand the scattering mechanism in the $PdSe_2$ samples.

The overall scattering rate for the state $|n\vec{k}\rangle$ is the sum of each scattering mechanism according to Matthiessen's rule

$$\tau^{-1}_{n\vec{k}} = \sum_m \int \frac{d^3\vec{q}}{V}\tau^{-1}_{n\vec{k}\to m\vec{k}+\vec{q}}$$

https://doi.org/10.1021/acsami.1c10500
ACS Appl. Mater. Interfaces 2021, 13, 37527−37534

where V is the volume of the first Brillouin zone. In addition, the elastic constant matrix, static dielectric matrix, and high-frequency dielectric matrix data are provided in Tables S2,S3.

■ ASSOCIATED CONTENT

Supporting Information

The Supporting Information is available free of charge at https://pubs.acs.org/doi/10.1021/acsami.1c10500.

AFM image of the exfoliated $PdSe_2$ flake and the corresponding thickness spectra (Figure S1), Raman spectra of the exfoliated 38 nm $PdSe_2$ flake (Figure S2), calculated electronic band structure of bulk $PdSe_2$ with a 0 eV band gap using PBE-SCAN+rVV10 functionals and its lattice constants (Figure S3), $\ln \frac{1}{R}$ versus $\frac{1000}{T}$ fitted by $\frac{1}{R} \propto \exp\left(\frac{-E_g}{2kT}\right)$ (Figure S4), calculated phonon dispersion of bulk $PdSe_2$ (Figure S5), linear MR along the b-axis at various temperatures from 3 to 300 K (Figure S6), gate voltage dependence of resistance under a zero magnetic field at various temperatures from 3 to 300 K (Figure S7), measured electron mobility for the a-axis as a function of temperature and electron mobility for the a-axis and b-axis from 3 to 40 K (Figure S8), calculated electron mobility as a function of electron concentration without the boundary effect and temperature-dependent electron mobility with various electron concentrations for the a-axis and b-axis without the boundary effect, which means we only consider acoustic deformation potential scattering and polar optical phonon scattering, (Figure S9), comparison of calculated lattice constants under different functionals (Table S1), elastic constant matrix (Table S2), and static dielectric matrix and high-frequency dielectric matrix (Table S3) (PDF)

■ AUTHOR INFORMATION

Corresponding Authors

Qijie Liang − *Department of Physics, National University of Singapore, Singapore 117551, Singapore; Songshan Lake Materials Laboratory, Songshan Lake Mat Lab, Dongguan 523808, China*; Email: liangqijie@sslab.org.cn

Andrew Thye Shen Wee − *Department of Physics, National University of Singapore, Singapore 117551, Singapore; Centre for Advanced 2D Materials and Graphene Research Centre, National University of Singapore, Singapore 117546, Singapore*; orcid.org/0000-0002-5828-4312; Email: phyweets@nus.edu.sg

Authors

Rui Zhu − *Department of Physics, National University of Singapore, Singapore 117551, Singapore*; orcid.org/0000-0003-4165-9568

Zhibin Gao − *Department of Physics, National University of Singapore, Singapore 117551, Singapore; State Key Laboratory for Mechanical Behavior of Materials, Xi'an Jiaotong University, Xi'an 710049, China*; orcid.org/0000-0002-6843-381X

Junxiong Hu − *Department of Physics, National University of Singapore, Singapore 117551, Singapore*

Jian-Sheng Wang − *Department of Physics, National University of Singapore, Singapore 117551, Singapore*

Cheng-Wei Qiu − *Department of Electrical and Computer Engineering, National University of Singapore, Singapore 117583, Singapore*

Complete contact information is available at: https://pubs.acs.org/10.1021/acsami.1c10500

Author Contributions

R.Z. conceived the idea and conducted the experiments. Z.G. performed the DFT calculations. R.Z., Z.G., Q.L., and A.T.S.W. wrote the manuscript. The manuscript was written through contributions of all authors. All authors have given approval to the final version of the manuscript. R.Z. and Z.G. contributed equally to this work.

Notes

The authors declare no competing financial interest.

■ ACKNOWLEDGMENTS

A.T.S.W. acknowledges funding support from the MOE Tier 2 grant MOE2017-T2-2-139. Z.G. and J.-S.W. acknowledge the financial support from the MOE tier 1 funding of Singapore with Grant No. R-144-000-427-114.

■ REFERENCES

(1) Daughton, J. M. GMR Applications. *J. Magn. Magn. Mater.* **1999**, *192*, 334−342.

(2) Velev, J.; Sabirianov, R. F.; Jaswal, S. S.; Tsymbal, E. Y. Ballistic Anisotropic Magnetoresistance. *Phys. Rev. Lett.* **2005**, *94*, 1−4.

(3) Fina, I.; Marti, X.; Yi, D.; Liu, J.; Chu, J. H.; Rayan-Serrao, C.; Suresha, S.; Shick, A. B.; Železný, J.; Jungwirth, T. Anisotropic Magnetoresistance in an Antiferromagnetic Semiconductor. *Nature. Commun.* **2014**, *5*, 1−8.

(4) Wang, H.; Lu, C.; Chen, J.; Liu, Y.; Yuan, S. L.; Cheong, S. W.; Dong, S.; Liu, J. M. Giant Anisotropic Magnetoresistance and Nonvolatile Memory in Canted Antiferromagnet Sr_2IrO_4. *Nat. Commun.* **2019**, *10*, 1−7.

(5) Yang, S. Y.; Noky, J.; Gayles, J.; Dejene, F. K.; Sun, Y.; Dörr, M.; Skourski, Y.; Felser, C.; Ali, M. N.; Liu, E. Field-Modulated Anomalous Hall Conductivity and Planar Hall Effect in $Co_3Sn_2S_2$ Nanoflakes. *Nano Lett.* **2020**, *20*, 7860−7867.

(6) Fan, L. Y.; Tang, F.; Meng, W. Z.; Zhao, W.; Zhang, L.; Han, Z. D.; Qian, B.; Jiang, X. F.; Zhang, X. M.; Fang, Y. Anisotropic and Extreme Magnetoresistance in the Magnetic Semimetal Candidate Erbium Monobismuthide. *Phys. Rev. B* **2020**, *102*, No. 104417.

(7) Perna, P.; Maccariello, D.; Ajejas, F.; Guerrero, R.; Méchin, L.; Flament, S.; Santamaria, J.; Miranda, R.; Camarero, J. Engineering Large Anisotropic Magnetoresistance in $La_{0.7}Sr_{0.3}MnO_3$ Films at Room Temperature. *Adv. Funct. Mater.* **2017**, *27*, 1−7.

(8) Zhao, C. J.; Ding, L.; Huangfu, J. S.; Zhang, J. Y.; Yu, G. H. Research Progress in Anisotropic Magnetoresistance. *Rare Met.* **2013**, *32*, 213−224.

(9) Tombros, N.; Jozsa, C.; Popinciuc, M.; Jonkman, H. T.; Van Wees, B. J. Electronic Spin Transport and Spin Precession in Single Graphene Layers at Room Temperature. *Nature* **2007**, *448*, 571−574.

(10) Novoselov, K. S.; Fal'Ko, V. I.; Colombo, L.; Gellert, P. R.; Schwab, M. G.; Kim, K. A Roadmap for Graphene. *Nature* **2012**, *490*, 192−200.

(11) Zhang, W.; Wong, P. K. J.; Zhu, R.; Van Der Wee, A. T. S. Waals Magnets: Wonder Building Blocks for Two-dimensional Spintronics? *InfoMat* **2019**, *1*, 479−495.

(12) Li, L.; Han, W.; Pi, L.; Niu, P.; Han, J.; Wang, C.; Su, B.; Li, H.; Xiong, J.; Bando, Y. Emerging In-plane Anisotropic Two-dimensional Materials. *InfoMat* **2019**, *1*, 54−73.

(13) Song, Q.; Pan, X.; Wang, H.; Zhang, K.; Tan, Q.; Li, P.; Wan, Y.; Wang, Y.; Xu, X.; Lin, M. The In-Plane Anisotropy of WTe_2 Investigated by Angle-Dependent and Polarized Raman Spectroscopy. *Sci. Rep.* **2016**, *6*, 1−9.

(14) Qiu, G.; Du, Y.; Charnas, A.; Zhou, H.; Jin, S.; Luo, Z.; Zemlyanov, D. Y.; Xu, X.; Cheng, G. J.; Ye, P. D. Observation of Optical and Electrical In-Plane Anisotropy in High-Mobility Few-Layer $ZrTe_5$. *Nano Lett.* **2016**, *16*, 7364−7369.
(15) Tian, Z.; Guo, C.; Zhao, M.; Li, R.; Xue, J. Two-Dimensional SnS: A Phosphorene Analogue with Strong In-Plane Electronic Anisotropy. *ACS Nano* **2017**, *11*, 2219−2226.
(16) Wang, H.; Chen, M. L.; Zhu, M.; Wang, Y.; Dong, B.; Sun, X.; Zhang, X.; Cao, S.; Li, X.; Huang, J. Gate Tunable Giant Anisotropic Resistance in Ultra-Thin GaTe. *Nat. Commun.* **2019**, *10*, 1−8.
(17) Oyedele, A. D.; Yang, S.; Liang, L.; Puretzky, A. A.; Wang, K.; Zhang, J.; Yu, P.; Pudasaini, P. R.; Ghosh, A. W.; Liu, Z. $PdSe_2$: Pentagonal Two-Dimensional Layers with High Air Stability for Electronics. *J. Am. Chem. Soc.* **2017**, *139*, 14090−14097.
(18) Mccann, E.; Kechedzhi, K.; Fala'Ko, V. I.; Suzuura, H.; Ando, T.; Altshuler, B. L. Weak-Localization Magnetoresistance and Valley Symmetry in Graphene. *Phys. Rev. Lett.* **2006**, *97*, 14−17.
(19) Lu, J.; Zhang, H.; Shi, W.; Wang, Z.; Zheng, Y.; Zhang, T.; Wang, N.; Tang, Z.; Sheng, P. Graphene Magnetoresistance Device in van Der Pauw Geometry. *Nano Lett.* **2011**, *11*, 2973−2977.
(20) Wang, H.; Chen, M.-L.; Zhu, M.; Wang, Y.; Dong, B.; Sun, X.; Zhang, X.; Cao, S.; Li, X.; Huang, J.; Zhang, L.; Liu, W.; Sun, D.; Ye, Y.; Song, K.; Wang, J.; Han, Y.; Yang, T.; Guo, H.; Qin, C.; Xiao, L.; Zhang, J.; Chen, J.; Han, Z.; Zhang, Z. Gate-Tunable Negative Longitudinal Magnetoresistance in the Predicted Type-II Weyl Semimetal WTe_2. *Nat. Commun.* **2016**, *7*, 1−6.
(21) Ali, M. N.; Xiong, J.; Flynn, S.; Tao, J.; Gibson, Q. D.; Schoop, L. M.; Liang, T.; Haldolaarachchige, N.; Hirschberger, M.; Ong, N. P. Large, Non-Saturating Magnetoresistance in WTe_2. *Nature* **2014**, *514*, 205−208.
(22) Zhang, Y.; Liu, J.; Wang, G.; Wang, W.; Xu, J.; Li, L. Negative Magnetoresistance Effect of $PtSe_2$ film in variable range hopping regime. *Appl. Phys. Lett.* **2020**, *116*, 213104.
(23) Zhang, Y.; Ning, H.; Li, Y.; Liu, Y.; Wang, J. Negative to Positive Crossover of the Magnetoresistance in Layered WS_2. *Appl. Phys. Lett.* **2016**, *108*, 153114.
(24) Dau, M. T.; Vergnaud, C.; Marty, A.; Rortais, F.; Beigné, C.; Boukari, H.; Bellet-Amalric, E.; Guigoz, V.; Renault, O.; Alvarez, C. Millimeter-Scale Layered $MoSe_2$ grown on sapphire and evidence for negative magnetoresistance. *Appl. Phys. Lett.* **2017**, *110*, No. 011909.
(25) Jiang, X. H.; Xiong, F.; Zhang, X. W.; Hua, Z. H.; Wang, Z. H.; Yang, S. G. Large Magnetoresistance and Hall Effect in Paramagnetic Black Phosphorus Synthesized from Red Phosphorus. *J. Phys. D: Appl. Phys.* **2018**, *51*, 195101.
(26) Telesio, F.; Hemsworth, N.; Dickerson, W.; Petrescu, M.; Tayari, V.; Yu, O.; Graf, D.; Serrano-Ruiz, M.; Caporali, M.; Peruzzini, M. Nonclassical Longitudinal Magnetoresistance in Anisotropic Black Phosphorus. *Phys. Status Solidi RRL* **2020**, *14*, No. 1900347.
(27) Chen, E.; Xu, W.; Chen, J.; Warner, J. H. 2D Layered Noble Metal Dichalcogenides (Pt, Pd, Se, S) for Electronics and Energy Applications. *Mater. Today Adv.* **2020**, *7*, No. 100076.
(28) Gao, Z.; Wang, J. S. Thermoelectric Penta-Silicene with a High Room-Temperature Figure of Merit. *ACS Appl. Mater. Inter.* **2020**, *12*, 14298−14307.
(29) Gao, Z.; Zhang, Z.; Liu, G.; Wang, J. S. Ultra-Low Lattice Thermal Conductivity of Monolayer Penta-Silicene and Penta-Germanene. *Phys. Chem. Chem. Phys.* **2019**, *21*, 26033−26040.
(30) Xie, C.; Jiang, S.; Gao, Y.; Hong, M.; Pan, S.; Zhao, J.; Zhang, Y. Giant Thickness-Tunable Bandgap and Robust Air Stability of 2D Palladium Diselenide. *Small* **2020**, *16*, No. 2000754.
(31) Liang, Q.; Wang, Q.; Zhang, Q.; Wei, J.; Lim, S. X.; Zhu, R.; Hu, J.; Wei, W.; Lee, C.; Sow, C. H. High-Performance, Room Temperature, Ultra-Broadband Photodetectors Based on Air-Stable $PdSe_2$. *Adv. Mater.* **2019**, *31*, 1−9.
(32) Luo, W.; Oyedele, A. D.; Gu, Y.; Li, T.; Wang, X.; Haglund, A. V.; Mandrus, D.; Puretzky, A. A.; Xiao, K.; Liang, L. Anisotropic Phonon Response of Few-Layer $PdSe_2$ under Uniaxial Strain. *Adv. Funct. Mater.* **2020**, *30*, No. 2003215.
(33) Liang, Q.; Zhang, Q.; Gou, J.; Song, T.; Arramel; Chen, H.; Yang, M.; Lim, S. X.; Wang, Q.; Zhu, R.; Yakovlev, N.; Tan, S. C.; Zhang, W.; Novoselov, K. S.; Wee, A. T. S. Performance Improvement by Ozone Treatment of 2D $PdSe_2$. *ACS Nano* **2020**, *14*, 5668−5677.
(34) Yu, J.; Kuang, X.; Gao, Y.; Wang, Y.; Chen, K.; Ding, Z.; Liu, J.; Cong, C.; He, J.; Liu, Z. Direct Observation of the Linear Dichroism Transition in Two-Dimensional Palladium Diselenide. *Nano Lett.* **2020**, *20*, 1172−1182.
(35) Pi, L.; Hu, C.; Shen, W.; Li, L.; Luo, P.; Hu, X.; Chen, P.; Li, D.; Li, Z.; Zhou, X. Highly In-Plane Anisotropic 2D PdSe2for Polarized Photodetection with Orientation Selectivity. *Adv. Funct. Mater.* **2021**, *31*, No. 2006774.
(36) Zhang, G.; Amani, M.; Chaturvedi, A.; Tan, C.; Bullock, J.; Song, X.; Kim, H.; Lien, D. H.; Scott, M. C.; Zhang, H. Optical and Electrical Properties of Two-Dimensional Palladium Diselenide. *Appl. Phys. Lett.* **2019**, *114*, 253102.
(37) Parish, M. M.; Littlewood, P. B. Non-Saturating Magnetoresistance in Heavily Disordered Semiconductors. *Nature* **2003**, *426*, 162−165.
(38) Li, H.; Wang, H. W.; He, H.; Wang, J.; Shen, S. Q. Giant Anisotropic Magnetoresistance and Planar Hall Effect in the Dirac Semimetal Cd_3As_2. *Phys. Rev. B* **2018**, *97*, 1−6.
(39) Kang, S.; Lee, D.; Kim, J.; Capasso, A.; Kang, H. S.; Park, J. W.; Lee, C. H.; Lee, G. H. 2D Semiconducting Materials for Electronic and Optoelectronic Applications: Potential and Challenge. *2D Materials* **2020**, *7*, No. 022003.
(40) Peng, H.; Yang, Z.-H.; Sun, J.; Perdew, J. P. SCAN+rVV10: A Promising van Der Waals Density Functional. *Phys Rev X* **2016**, *6*, 1−8.
(41) Soulard, C.; Rocquefelte, X.; Petit, P. E.; Evain, M.; Jobic, S.; Itié, J. P.; Munsch, P.; Koo, H. J.; Whangbo, M. H. Experimental and Theoretical Investigation on the Relative Stability of the PdS_2- and Pyrite-Type Structures of $PdSe_2$. *Inorg. Chem.* **2004**, *43*, 1943−1949.
(42) Saputra, R. Self-interaction-corrected density-functional formalism. *J. Chem. Info. Model.* **2019**, *53*, 1689−1699.
(43) Botana, A. S.; Norman, M. R. Electronic Structure and Magnetism of Transition Metal Dihalides: Bulk to Monolayer. *Phys. Rev. Materials* **2019**, *3*, No. 044001.
(44) Averitt, R. D.; Sarkar, D.; Halas, N. J. Plasmon Resonance Shifts of Au-Coated Au_2S nanoshells: Insight into multicomponent nanoparticle growth. *Phys. Rev. Lett.* **1997**, *78*, 4217−4220.
(45) Bardeen, J.; Shockley, W. Deformation Potentials and Mobilities in Non-Polar Crystals. *Phys. Rev.* **1950**, *80*, 72−80.
(46) Brorsen, K. R.; Yang, Y.; Hammes-Schiffer, S. Multicomponent Density Functional Theory: Impact of Nuclear Quantum Effects on Proton Affinities and Geometries. *J. Phys. Chem. Lett.* **2017**, *8*, 3488−3493.
(47) Najmaei, S.; Liu, Z.; Zhou, W.; Zou, X.; Shi, G.; Lei, S.; Yakobson, B. I.; Idrobo, J. C.; Ajayan, P. M.; Lou, J. Vapour Phase Growth and Grain Boundary Structure of Molybdenum Disulphide Atomic Layers. *Nat. Mater.* **2013**, *12*, 754−759.

https://doi.org/10.1021/acsami.1c10500
ACS Appl. Mater. Interfaces 2021, 13, 37527−37534